Jour. Korean Inst. Mining Geol.
Vol. 23, No. 4, p. 393-409, 1990.

Synthetic Seismograms of Non-geometric S* and P* Waves Using the Reflectivity Method

Dong Hee Hong* and Chang Eob Baag*

ABSTRACT : Synthetic seismograms and deduced characteristic properties of the non-geometrical S* and P* waves are presented. These waves are excited on the free surface or an interface between two different media by an inhomogeneous P wave from a point source nearby, and propagate as homogeneous waves in the media. Synthetic seismograms are computed using an extended reflectivity method designed for buried source and receiver. An efficient computational procedure for propagator matrices of layers is devised to reduce the computational time and the RAM memory size in the implementation of the reflectivity method. Radiation patterns are obtained from the particle motions of the four types of the "*" waves, i.e., the S* wave generated near the free surface, and the reflected S*, transmitted S* and transmitted P* waves generated near an interface. Some patterns show polarity changes of displacements and others reveal monotonic or non-monotonic variation of amplitude depending on the velocity structure. The decaying trend of amplitude with increasing epicentral distance are also shown for the head wave type of the "*" waves.

INTRODUCTION

A numerical investigation of Lamb's problem for an explosive isotropic point source at a small distance from the free surface in a homogeneous, ideally elastic half-space was undertaken by Hron and Mikhailenko (Mikhailenko and Hron, 1980 ; Hron and Mikhailenko, 1981). As results of a numerical elastic modelling scheme using the Alekseev and Mikhailenko method (Alekseev and Mikhailenko, 1980) which involves finite difference method (Alterman and Loewenthal, 1972 ; Boore, 1972 ; Alford et al., 1974 ; Kelly et al., 1976) and finite Hankel transforms, a new and very prominent non-geometrical arrival in their theoretical seismograms was reported. According to their analysis the new arrival, tentatively denoted as S*, has following characteristic properties : As the depth of the source beneath the free surface decrease linearly, the amplitude of the S* wave increases exponentially, if the depth is smaller than one predominant wavelength of the source pulse. For a given epicentral distance (offset), the amplitude of the wave increases almost linearly with increasing receiver depth, at least in a region close to the free surface. The propagaion of the wave is confined to the region between the free surface and a concial surface which is symmetric about the vertical axis passing through the source. The angle of the cone is given by $\chi^* = \sin^{-1}(\beta / \alpha)$, where α and β are the P and S wave velocities, respectively, in the elastic half-space. S* appears to originate at the vertex O* of the above mentioned cone (Fig. 1) and propagates with the shear wave velocity. The particle motion of the wave is linearly polarized in a plane normal to the direction of propagation indicating that S* travels as an ordinary shear wave and hence is subject to reflection, transmission, and conversion at interfaces as an SV wave.

Hron and Mikhailenko (1981) suggested that the S* may be physically interpreted as the result of the interaction between the free surface near the source and inhomogeneous plane waves which exist in the Sommerfeld integral representation of spherical wave front radiated by an explosive point source. Also indicated was that the contribution of the S* arrival to the reflected PS wave field may be obtained mathematically as a saddle-point approximation of a contour integral in the complex plane of horizontal slowness p. This saddle point lies on the real axis in the range $1/\alpha < p < 1/\beta$. This integral must be considered for shallow explosive sources as it provides a significant contribution to the line integral representing the reflected PS

This paper was supported by NON DIRECTED RESEARCH FUND, Korea Research Foundation, 1989.

* Department of Geological Sciences, Seoul National University, Seoul 151-742, Korea.

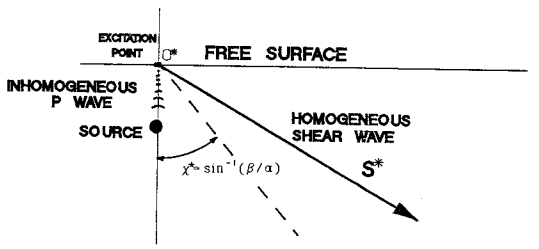

Fig. 1. Excitation of the S* by compressional wave source located at very shallow depth and the permissible region for propagation path of the S* wave. The wave is confined to the region between the free surface and the dashed line defined by a directional angle $\chi^* = \sin^{-1}(\beta / \alpha)$. α and β are wave velocities of P and S waves in the half-space.

wave field. The importance of such a shallow sources has been already anticipated by Lapwood (1949).

Daley and Hron (1983a) developed a high frequency approximation to the amplitude of the S* using a saddle-point approximation of the integral representing the total field of the reflected PS wave. They presented formulas for the radiation pattern in addition to the expressions of the radial and vertical displacements of the S* wave. Daley and Hron (1983b) also presented a high frequency approximation for the non-geometrical "*" waves generated by highly concentrated sources adjacent to the interfaces between two different elastic media rather than free surface following their detection in the field data obtained by Gutowski et al. (1984). According to the two papers of Daley and Hron (1983 a and b), the "*" waves in the integral representation of the reflected and transmitted wave fields are associated with saddle-point contributions of the contour integration circumventing branch point singularities in the complex plane of ray parameter p in which the Sommerfeld or Weyl integral should be evaluated. They mentioned that their formulas are for easy incorporation into any theoretical seismogram computation based on the ray theory.

Recently, Kim and Behrens (1985, 1986) ascertained the results obtained by the numerical methods mentioned above by means of model-seismic experiments based on two-dimensional physical models.

The S waves have received little attention from seismologist in comparison to studies of P waves, even though S waves contain independent information on the geologic structures. The S waves attenuate rapidly than P waves and their responses are more sensitive in weathered medium. And the ratio of P and S wave velocities can be used as the parameters indicating the existence of the hydrocarbon directly, since it shows more sensitive response in the media including oil and gas. Additionally it would be used to discriminate rock lithology effectively. Since the use of the shallow explosive sources for seismic exploration is favourable for the generation of non-geometric "*" arrivals, the ability to synthesize them is useful for interpreting observed seismograms. Indeed, all preliminary studies indicate that the S* arrivals may be used as an inexpensive and convenient source in shear wave prospecting (Bortfeld and Fertig, 1982). Actually the "*" signals from shallow sources or sources near layer interfaces are important because they have very large amplitudes.

Up to this time the study of "*" arrivals has been done by only a few authors as stated above, and many problems remain to be investigated. The Alekseev-Mikhailenko method is expensive for the synthesis of the "*" waves and may not convenient for the routine interpretation of recorded seismograms. Sometimes we need to compute other phases of distinct ray and surface waves together with the "*" waves.

The high frequency approximation method of Daley and Hron (1983 a and b) is not mathematically justified for the frequencies at the vicinity of a distinct ray and surface waves because integral solutions have rapid variations in the vicinity of branch cut singularities. None of these methods include computations of the "*" waves suffered by the medium anelasticity which can be an important factor for interpretation of observed data.

In order to overcome some of these limitations of previous methods for synthesis of "*" waves, and to provide more realistic interpretations for the structure dependencies of the waves, an extended reflectivity method is used in this paper. Wavenumber integration is done along the real axis of the complex wavenumber plane, and anelasticity is included using complex velocities in all regions of the structural model. Using the method, synthetics of the "*" waves are generated, and the effects of source depth, receiver location, and velocity structure variations on the behaviour of the wave are examined to provide a basis for interpretation of observed seismograms.

EXCITATION OF THE NON-GEOMETRICAL "*" WAVES

The term "*" waves refer to the converted compressional and shear waves of the incident inhomogeneous compressional P-wave by interactions with free surface or layer interfaces. In a horizontally layered medium, the vertical wavenumber of a wave component

$$\psi(\bar{k},\omega)=EXP[i(\bar{k}\cdot\bar{r}-\omega t)] \quad (1)$$

is expressed as

$$k_z=\omega(1/\upsilon^2-1/c^2)^{1/2} \quad (2)$$

where υ and c are wave velocity and horizontal phase velocity, respectively. If the phase velocity of a wave is greater than the shear wave velocity and less than the P wave velocity in a layer, then the vertical wavenumbers of P and S waves are

$$\begin{aligned} K_z^{\alpha} &= \omega(1/\alpha^2-1/c^2)^{1/2}=iA \\ K_z^{\beta} &= \omega(1/\beta^2-1/c^2)^{1/2} \end{aligned} \quad (3)$$

where, α and β are velocities of P and S waves in the layer, and A is a positive real number. Then the wave components of the P and S waves become

$$\begin{aligned} \psi^{\alpha}(\bar{k},\omega) &= EXP[i(k_x x-\omega t)]\cdot EXP(-Az) \\ \psi^{\beta}(\bar{k},\omega) &= EXP[i(k_x x+k_z^{\beta}-\omega t)] \end{aligned} \quad (4)$$

The P wave is an inhomogeneous wave which amplitude decays exponentially with depth, but the wave function of the S wave indicates a homogeneous wave. Thus, if the P-wave source is very close to an interface, the incident inhomogeneous P wave can be reflected as a homogeneous S wave from the interface. This reflected wave, S*, is a shear wave which has non-geometrical ray path and differs from the geometrically reflected PS wave because the former is excited by an inhomogeneous P-wave (Fig. 2). The schematic diagram for the source-receiver configuration for the excitation of the non-geometric shear wave, i.e., S* is given in Fig. 2. There are four predominant arrivals : the direct compressional wave (P), the reflected compressional wave (PP), the converted shear wave with geometrical ray path (PS), and the non-geometric shear wave (S*). Three phases except S* propagate along the geometrical ray paths controlled by Snell's law.

Similarly, after being radiated as an inhomogeneous P wave from an explosive source adjacent to a plane interface, the wave field transmitted across the interface from a relatively higher velocity elastic half-space into a next medium of lower velocity can be the converted homogeneous P and S waves. In this case, β in the equation (3) and (4) is replaced by α_2 or β_2 correponding to velocities of P and S waves, respectively, in the second medium. Compared with the reflected wave field including one non-geometrical S* arrival only, there are four non-geometrical "*" waves in transmitted wave fields: the converted compressional wave ($P_1P_2^*$), the converted shear wave ($P_1S_2^*$), and two converted shear waves of head wave type

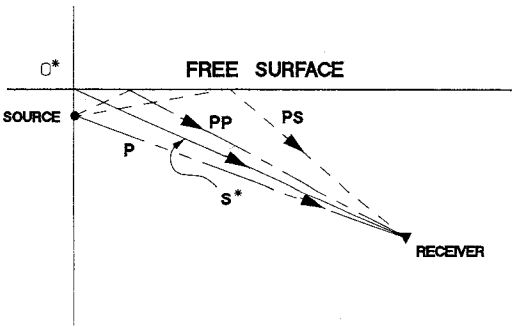

Fig. 2. Schematic diagram for the source-receiver configuration and ray paths of the non-geometrical S* wave and associated body waves. P ; direct compressional wave, PP ; reflected compressional wave, PS ; converted shear wave, and S* ;converted shear wave with non-geometric ray path.

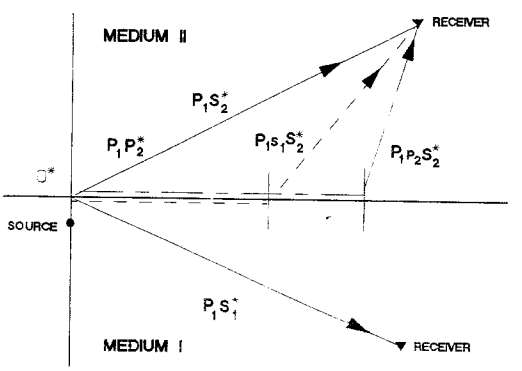

Fig. 3. Schematic diagram for ray paths of all the possible non-geometric "*" arrivals in reflected and transmitted wave fields. P and S is for the P and S wave, respectively. p and s in small letter represent horizontal propagation along the interface. Subscript 1 and 2 indicate propagation of the wave in the medium I and II, respectively.

($P_1s_1S_2^*$,$P_1p_2S_2^*$). Subscripts 1 and 2 indicate the first medium where the source is located and the second medium of lower velocity, respectively. The schematic diagram for ray paths of the waves is given in Fig. 3. These converted non-geometrical "*" waves would have amplitudes as large as those of other body waves, since these propagate as ordinary compressional and shear waves after reflected or transmitted. Therefore, the contributions of these waves are much significant in the total wave fields in particular situations.

In summary, the "*" arrivals are homogeneous waves generated by an inhomogeneous P wave source located near a medium boundary. Therefore, these waves propagate along non-geometrical ray paths, and may give some laborious work in interpreting observed seismograms and field data.

COMPUTATIONAL METHOD

Based on propagator matrix of Haskell (1953, 1960, 1962), Fuchs (1968, 1971) originated the reflectivity method for computation of synthetic seismograms in layered media. Numerical integration is done along the real axis of the complex wavenumber plane and is followed by the inverse Fourier transform over frequency to get seismograms in time domain. Both of the source and receiver was put at the free surface. The method generates waves which reflected from a stack of layers at depth. Hence only transmissions are allowed in the layer between the free surface and a specified stack of layers at depth. Using Harkrider's matrix formulation (Harkrider, 1964, 1970) and matrix manipulation techniques of Watson (1970) and Abo-zena (1971), Kind (1978) extened the Fuch's method to the source at depth and allowed multiple reflections in the whole layered structure including layers near the free surface.

Baag and Baag (1988) revised the extended reflectivity method for both of the source and receiver at depth to compute seismograms from boreholes, and eliminated numerical instability problems which is resulting from additional matrix multiplications due to the receiver at depth and is serious for computation of inhomogeneous waves. Since non-geometrical "*" waves are usually observed in data from a receiver installed in a borehole, we use this extended reflectivity method for a receiver at depth (Baag and Baag, 1988) to compute the waves. A brief explanation on the essence of the method and some computational techniques designed in the current study are given as follows :

The radial and vertical components, $V_r\ (Z_R)$ and $V_z\ (Z_R)$, of non-dimensional displacement velocities, i.e., the ratios of displacement velocities to the horizontal phase velocity in the P-SV-Rayleigh wave system are given as matrix formula,

$$V_r\ (Z_R \mid Z_R<Z_s)=\frac{1}{R_{11}}(R_{11},\ R_{12},\ R_{13},\ R_{15},\ R_{16})^{HS}\begin{pmatrix} M_2 & M_1 & 0 & 0 \\ M_3 & 0 & M_1 & 0 \\ M_4 & M_3 & M_2 & M_1 \\ 0 & M_4 & 0_2 & M_2 \\ 0 & 0 & M_4 & M_3 \end{pmatrix}^{SRF}\cdot S$$

$$V_z\ (Z_R \mid Z_R<Z_s)=\frac{1}{R_{11}}(R_{11},\ R_{12},\ R_{13},\ R_{15},\ R_{16})^{HS}\begin{pmatrix} N_2 & N_1 & 0 & 0 \\ N_3 & 0 & N_1 & 0 \\ N_4 & N_3 & N_2 & N_1 \\ 0 & N_4 & 0 & N_2 \\ 0 & 0 & N_4 & N_3 \end{pmatrix}^{SRF}\cdot S \qquad (5)$$

for the case of receiver above source, where

$$\begin{pmatrix} M_1 \\ M_2 \\ M_3 \\ M_4 \end{pmatrix}^{SRF}=\begin{pmatrix} A_{12} & A_{13} & A_{14} \\ A_{22} & A_{23} & A_{24} \\ A_{32} & A_{33} & A_{34} \\ A_{42} & A_{43} & A_{44} \end{pmatrix}^{SR}\begin{pmatrix} R_{11} \\ R_{21} \\ R_{31} \end{pmatrix}^{RF}$$

$$\begin{pmatrix} N_1 \\ N_2 \\ N_3 \\ N_4 \end{pmatrix}^{SRF}=\begin{pmatrix} A_{11} & A_{13} & A_{14} \\ A_{21} & A_{23} & A_{24} \\ A_{31} & A_{33} & A_{34} \\ A_{41} & A_{43} & A_{44} \end{pmatrix}^{SR}\begin{pmatrix} R_{11} \\ R_{31} \\ R_{51} \end{pmatrix}^{RF}$$

and for the situation of receiver below the source

$$\begin{pmatrix} V_r(Z_R \mid Z_R>Z_S) \\ V_z(Z_R \mid Z_R>Z_S) \end{pmatrix}=\frac{1}{R_{11}}\begin{pmatrix} R_{13}, & R_{15}, & R_{16}, & 0 \\ -R_{12}, & -R_{13}, & 0 & R_{16} \end{pmatrix}^{HR}\cdot A^{RS}\cdot L^{SF}\cdot S \qquad (6)$$

where the matrix L is given as

$$L=\begin{pmatrix} R_{31} & -R_{21} & R_{11} & 0 \\ R_{51} & -R_{31} & 0 & R_{11} \\ R_{61} & 0 & -R_{31} & R_{21} \\ 0 & R_{61} & -R_{51} & R_{31} \end{pmatrix}$$

$R[6\times6]$ and $A[4\times4]$ are compound and Haskell layer matrix elements, respectively. Superscripts F, S, R, and H assigned to the matrices are for the propagation direction and depth ranges of the matrices. They indicate the free surface, source depth, receiver depth, and the half-space depth.

As a first step to obtain the final time series, radial and vertical displacements $U_r\ (Z_R)$ and $U_z\ (Z_R)$, both of the functions $V_r\ (Z_R)$ and $V_z\ (Z_R)$ in the equations (5) and (6) are inversely transformed from the wavenumber domain to radial

space domain. The transform is performed by numerical integration along the real axis in the complex wavenumber domain. The transformation integrals in the wavenumber domain for isotropic explosion source are

$$U_r(r,\ \omega;\ Z_R) = -\int_{k_1}^{k_2} \frac{1}{k} V_r(Z_R)\ J_1(kr)\ dk$$
$$U_z(r,\ \omega;\ Z_R) = -\int_{k_1}^{k_2} \frac{1}{k} V_z(Z_R)\ J_0(kr)\ dk \quad (7)$$

Here, Jn $(n=0,1)$ is the Bessel functions of n'th order. The integrations are limited to a finite wavenumber window or finite slowness window depending on the research interests. We chose the slowness window scheme in this study in order to pick up specific seismic phase only. And we can apply the cosine taper to both ends of the finite slowness window in order to reduce the numerical errors caused by truncation effects.

Since the method uses effective wave velocities

$$k=\frac{\omega}{C_o}\left[1-\frac{\ln(\gamma\ \omega/\omega_c)}{\pi Q}-\frac{i}{2Q}\right] \quad (8)$$

to include anelastic property of the medium, poles and branch points of the integrands are shifted off the real axis of the complex wavenumber or slowness axis. Here γ is Euler-Masheroni constant and ω_c is a cut-off frequency. Schematic diagram of integration paths and ranges for the non-geometric "*" waves are shown in Fig. 4.

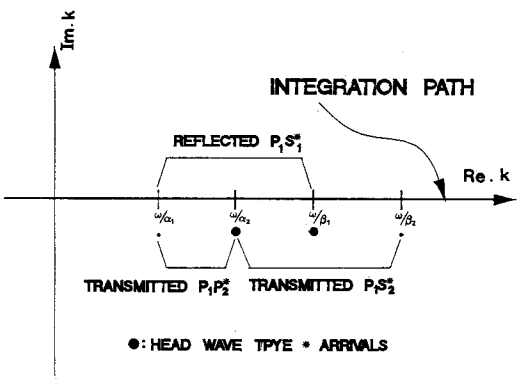

Fig. 4. The integration paths and ranges in the wavenumber integration for generation of all the non-geometric "*" arrivals in the complex wavenumber plane for the structural geometry of Fig. 3. The possible range for the individual "*" arrival is confined by the blanket. Subscript 1 and 2 indicate upper and lower mediums. Re. k and Im. k mean the real and imaginary values of the wavenumber.

Next step to get seismograms is the inverse Fourier transform over frequency for the results obtained from the equation (7),

$$U(r,t)=\frac{1}{2\pi}\int_{-\infty}^{\infty} U(r,\omega)\ exp(i\omega t)\ d\omega \quad (9)$$

Where $U(r, w)$ represents U_r or U_z in the equation (7). In actual computation discrete Fast Fourier transformation algorithm is used to evaluate the integral numerically.

The calculation of individual layer matrix elements and their multiplications are usually the most time-consuming part in the numerical computaion of the reflectivity method, since it has to be done typically for several hundred slowness points and several tens to hundreds of frequencies. Even though the computation time may be reduced by vectorizing the algorithm of the method and by using parallel or vector processors (Sandmeier and Wenzel, 1986), some useful techniques in layer matrix computations can be applied in order to reduce more the computational time avoiding some unnecessary calculations. The techniques and procedures of matrix element computations are shown in the next a few paragraphs.

For the convenience we divide the vertical model structure into three parts, as we see in Fig. 5. The first one is 'a' between the free surface and the uppermost one of the source and receiver. The second one is 'b' between the

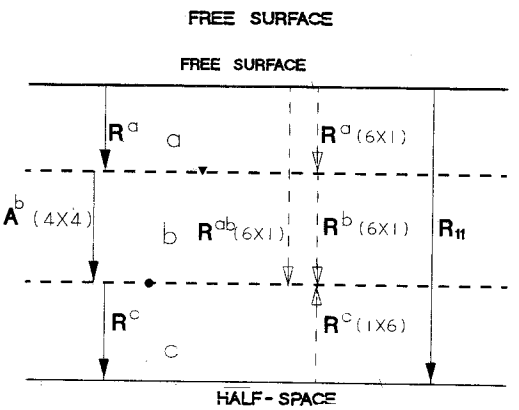

Fig. 5. Diagram of matrix multiplication procedure; closed circle and triangle indicate the source or receiver depth. Each portion divided by the source and receiver depth can be calculated separately. R and A are the product of compound matrix and Haskell layer matrix, respectively. The numerical numbers in the parentheses are the dimensions of the matrices. The dashed limes with open arrows indicate the matrix multiplication direction and the closed arrow with solid line indicate the propagation direction of the vector property.

source and receiver, and the last one is 'c', the layers from the half-space to the lowest one of the source and receiver.

In the equation (5) and (6), we need a [6×1] column vectors of the compound layer matrix in part 'a', a [1×6] row vectors of the compound layer matrix in part 'c', a [4×4] Haskell matrix in part 'b', and one compound layer matrix element R_{11} throughout all the layers. The column vector in part 'a', and row vector in part 'c' is to be represented

$$R^a[6\times1] = R^{m-1}[6\times6]\cdot R^{m-2}[6\times6]\cdots R^1[6\times1]$$
$$R^c[1\times6] = R^L[1\times6]\cdots R^{n+1}[6\times6]\cdot R^n[6\times6] \quad (10)$$

where the superscript indicates the sequential ID number of each layer counting from the surface layer. The superscript m and n indicate the layer just above the shallower one and the deeper one, respectively, of the source and the receiver. The superscript L is for the half-space.

In order to get the component R_{11} of the equation (5) and (6), we first compute $R^{ab}[6\times1]$ and combine the result with $R^c[1\times6]$ in the equation (10). In the calculation of the compound matrix $R^{ab}[6\times1]$, we should store the compound matrix elements $R^a[6\times1]$ when the interface between the part 'a' and 'b' is passed in the procedure of successive matrix multiplications downwards from the surface layer. Eventually, the computation of the compound layer matrix is separated into R^{ab} and R^c, above and below the lowest one of the source and receiver. The matrix element R_{11} can be obtained by multiplication R^c with R^{ab}

$$R_{11}=R^c[1\times6]\cdot R^{ab}[6\times1] \quad (11)$$

$$R^{ab}[6\times1] = R^{n-1}[6\times6]\cdot R^{n-2}[6\times6]\cdots R^n[6\times6] \cdots R^1[6\times1] \quad (12)$$

For the Haskell matrix A in the region 'b', we have to compute all the [4×4] elements

$$A^b[4\times4] = A^{n-1}[4\times4]\cdot A^{n-2}[4\times4]\cdots A^m[4\times4] \quad (13)$$

These schemes separate completely matrix computation processes into parts depending on the location of the source and receiver depth. Matrix multiplication sequences are illustrated in Fig. 5. The open arrows indicate the matrix multiplication direction and closed arrow indicate propagation direction of vector property.

SYNTHETIC SEISMOGRAMS

Using the extended reflectivity method, synthetic seismograms of "*" arrivals and associated waves are computed for an isotropic explosion source in plane layered structure in order to ascertain the general dependence of "*" arrivals on source depth, epicentral distance, and receiver depth. In most calculations 128 frequency points are used. The time increment for synthetic wave forms is 0.004 seconds for the applications of practical seismic explorations. The waveform of Fig. 6 which is the source time function convolved with the instrument response of the receiver is used for all of the seismograms in this study. The frequency independent seismic quality factor Q for the seismic wave attenuation is included in the computations. The seismograms consist of radial and vertical displacement and each seismogram in a plot has the same amplitude scale in order to facilitate comparisons.

Since the primary interest is not concerned with observation aspects but with the excitation and propagation properties of the non-geometrical "*" arrivals with respect to elastic parameters and the geometry of the source and receivers, the model considered is kept simple. In this study, we consider two models consisting of one elastic half-space and two half-spaces in welded contact. The first model is for the geometrical waves and the non-geometrical S* wave reflected by the free surface and the second one is for the transmitted waves and non-geometrical "*" waves in a rough sense.

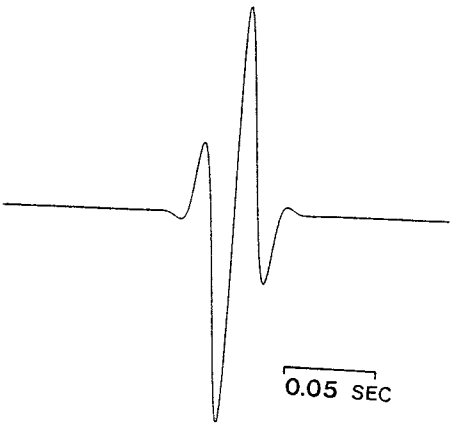

Fig. 6. The combined time function of the source and instrument used in the computation of synthetic seismograms. Amplitude unit is arbitrary.

General Waveform of Reflected S* Arrival

An isotropic homogeneous half-space was chosen and defined by the elastic parameters α, β, ρ and Q; the compressional and shear wave velocities, volume density, and seismic quality factor for attenuation which are given in Table 1. The ratio of β/α was set equal to 0.5. Units for dimension and time are given in metres and seconds.

Since the velocity model is defined as a half-space structure, the seismograms consist of direct wave and reflected waves generated by subsurface source. In order to deduce the fundamental properties of the S* wave with respect to source depth, we place a single receiver in the half-space at an epicentral distance 800m and at depth 250m. The large epicentral distance allows the time for propagating S* wave to be separated from shear body wave of the converted PS wave. The specified depth of the receiver makes the Rayleigh wave attenuate largely and the amplitude of the S* wave become comparable to those of P, PP, and PS arrivals. In general it is known that the Rayleigh wave shows an exponential decay of amplitude with increasing receiver depth. Since the propagation velocity of the Rayleigh wave is about 0.93β in this model shear waves can be separated in time from the Rayleigh wave. Therefore, the attenuated Rayleigh wave will not appreciably affect measurements of the S* arrivals at the prescribed positions of receivers.

Fig. 7 shows the radial and vertical components of the synthetics for ten source depths. The shallowest source is put at 5m below the free surface and nine other sources are distributed down to 200m depth with variable depth interval. The slowness range for numerical integration is between 0.2 sec/km and 0.5 sec/km, and cosine taper of 0.005 sec/km length is applied to both ends of the slowness window to reduce numerical errors of truncation effects in the

Table 1. Parameters of the medium.

P-velocity	S-velocity	density	Q-value(P)	Q-value(S)
4.0 km/sec	2.0 km/sec	1.0 g/cm^3	600	300

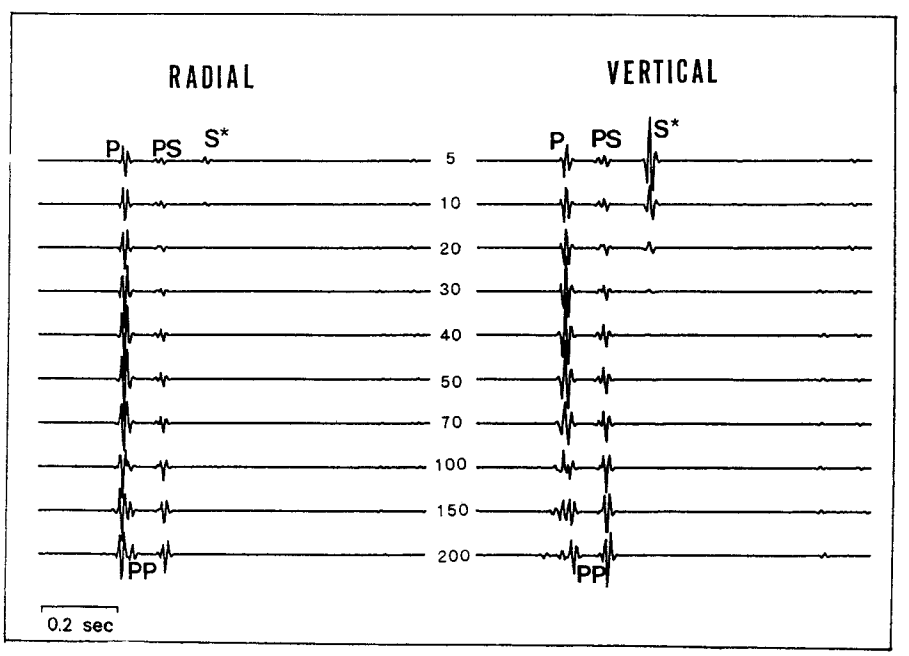

Fig. 7. Synthetic seismograms showing the amplitude variations of body waves including S* with increasing source depth. The receiver is located at epicentral distance 800m and at depth 250m from the surface. The number assigned to each trace is the source depth in metres. The initial phase is the direct P. PP and PS are the reflected P and converted S at the free surface.

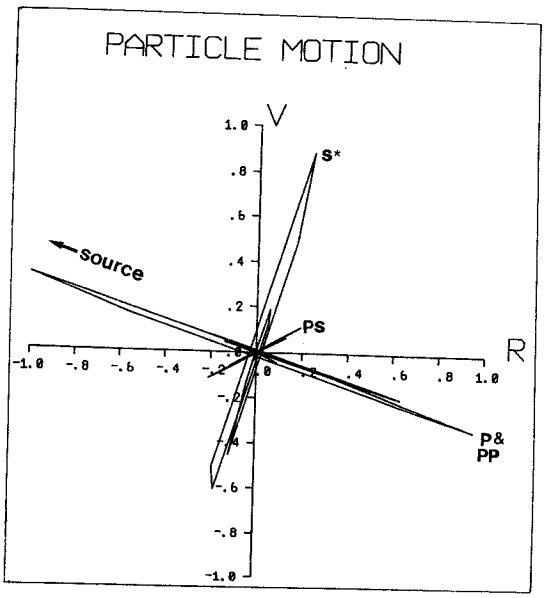

Fig. 8. The particle motion of S* wave and associated body waves for a receiver at epicentral distance 800m and depth 250m. The waves are generated by the source at 5m source depth. V and R indicate the vertical and radial components of the displacements. The amplitudes are normalized by that of the P wave and the arrow indicate the source position. Note that the motions of P and PP can not be distinguished for shallow source depth.

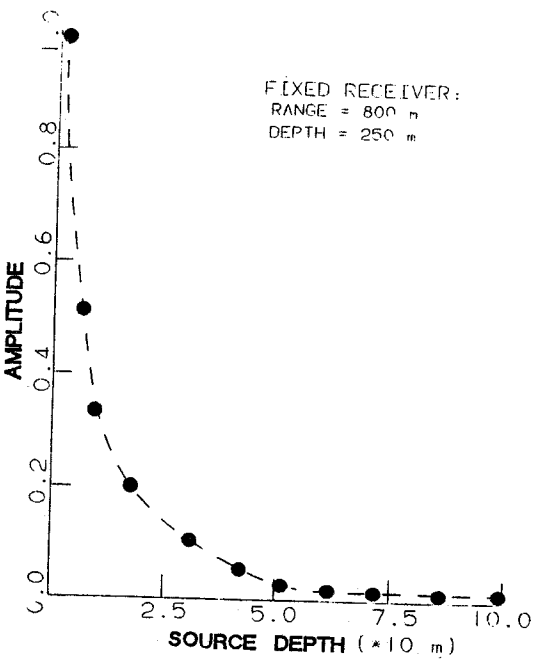

Fig. 9. Displacement amplitudes of S* versus source depth derived from the particle motion diagrams in Fig. 8. The amplitude is normalized by that for the source at depth 5m.

Bessel-Fourier transformation. This scheme of source configuration can give the behaviour of reflected S* in variation of the source depth. The arrival times of the direct P, the reflected PP, the converted PS, and the reflected S* phases are indicated by P, PP, PS, and S*, respectively. The direct P wave arrives about the same time as the reflected PP wave for shallow source depth, but they are separated with increaing source depth. The combined paticle motions of the reflected S* and other body waves over a time window of about 0.4 seconds starting with the theoretical P arrival time are depicted in Fig. 8 for the seismogram of 5m source depth given in Fig. 7. We can see that the particle motion of the S* wave is highly rectilinear as expected for an ordinary body wave and consistent with the shear wave generated from the position directly above the point source in the model geometry. Then we can deduce that the excitation point of the S* wave is the point directly above the source (Fig. 1). It should be noted that the vertically positive component in the Figure registers the upward displacement, and the radially negative component is for the displacement toward the source.

From the particle motion diagram of the S* wave in each seismogram of Fig. 7, we see that the displacement amplitudes of the wave decay with the source depth, and that the directions of the rectilinear particle motions are all the same for different source depth cases. The amplitude variation is displayed as a function of source depth in Fig. 9. It is clear that the best fit to the function is $exp\ (-Ah)$ (Gutowski et. al, 1984). Here, A is a constant defined by the elastic parameters of the medium and h is the source depth. As the inhomogeneous wave characterized by exponential amplitude decay along the direction of propagation was presented in mathematical representation of the spherical wave in the form of Sommerfeld integral (Aki and Richards, 1980), the excitation of the S* wave may be explained by conversion of the inhomogeneous wave energy to an ordinary shear wave at the point directly above the point

source. In order words, the energy of the inhomogeneous wave with the slowness range of $1/\alpha < p < 1/\beta$ which is radiated from the source reaches the surface after decaying along its propagation direction and converted to homogeneous S wave by reflection mechanism. Thus the amplitude of the S* wave decays with source depth.

In order to see the effect of epicentral distances on the S* wave, synthetics are computed using the structure model given in Table 1. The source is buried at 5m depth from the surface. The epicentral distances of the receivers are ranging from 550m to 1000m with 50m interval and fixed at 250m depth. In Fig.10(A), the degree of the arrival time delay of the S* wave is greater than that of the P or PS phases with increasing epicentral distance of ten receivers. Fig. 10 (B) for the source depth of 10m also shows similar features. The relative displacement amplitudes of the S* wave among other phases for 5m source depth is greater than those for 10m source depth. Thus we see that the S* wave is a shear body wave and its amplitude depends on the source depth.

The almost linear increase of the amplitude of the S* wave with increasing receiver depth is shown in Fig. 11. The source is located at 5m away from the surface in the half-space given in Table 1, and the epicentral distance is fixed at 800m from the source. The receiver depths of the individual traces are 20, 50, 100, 150, and 200, respectively. From the seismogram of the receiver at the free surface in Fig. 11, we can not see the S* wave but the Rayleigh wave denoted by R arrives with large amplitude. As the receiver become deeper, the amplitude of the S* wave increases and Rayleigh wave disappears. The latest arrivals of small amplitude are noises caused by truncaion of the slowness window in the numerical integration procedure.

Radiation Patterns of the Reflected S*

In order to examine the radiation pattern of the S*, an isotropic explosive point source is fixed at 5m below the free surface. Receivers are distributed on a wide quarter circle of radius 840m from the origin O* in a vertical section. The angular position of each receiver is measured from the downward vertical in the interval

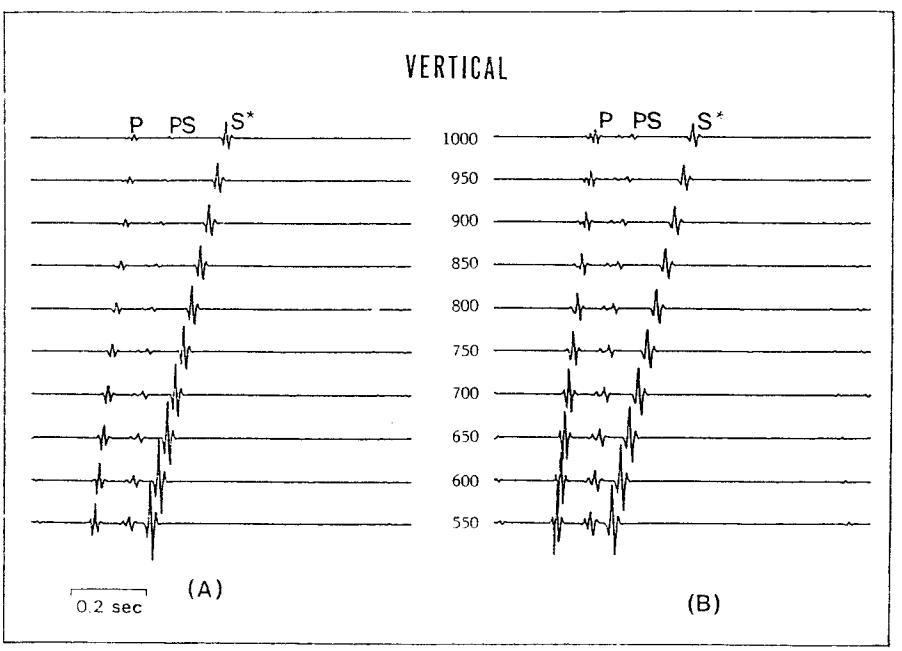

Fig. 10. Vertical displacement traces for the receiver depth of 250m. The structural model used is a half-space model given in Table 1. The numerical number assigned to each trace indicates epicentral distance in meter unit. The traces of part (A) is for the source at depth of 5m and those of part (B) for the source at 10m depth. Different scale factors were used for seismograms in parts (A) and (B).

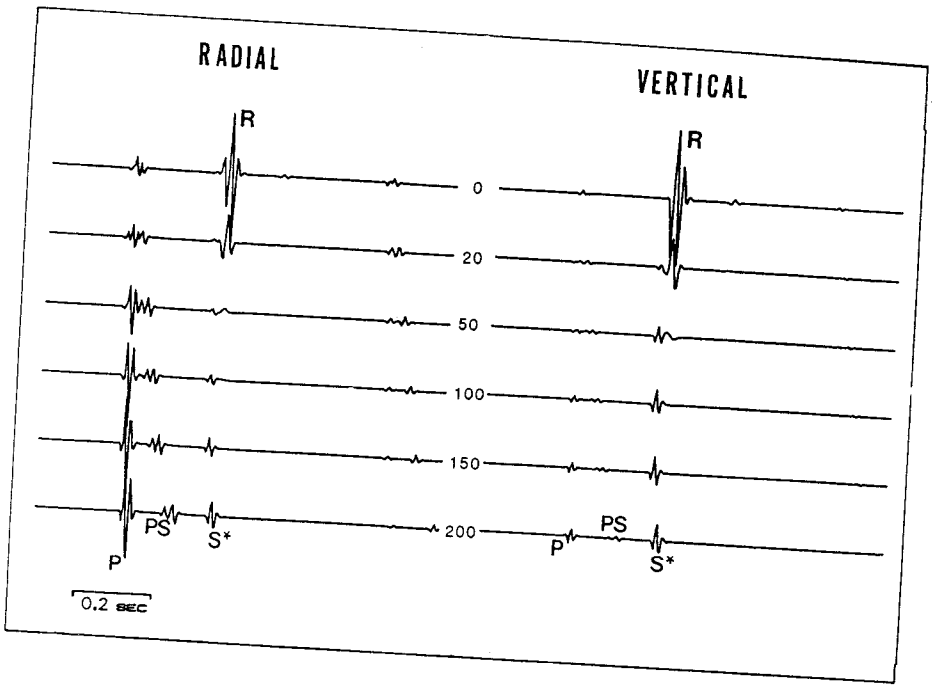

Fig. 11. Variations of synthetic seismograms with increasing receiver depth. The source depth and epicentral distance are fixed at 5m and 800m, respectively. The structure model given in Table 1 is used. The numerical number in each trace indicates receiver depth in meter from the free surface. The Rayleigh wave is denoted by R.

of 10 degrees. Fig. 12 displays the radial and vertical components of synthetics obtained by these receivers. The prominent emergent arrival on the 90° trace at about 0.42 second is Rayleigh wave denoted by R. The wave with sufficient energy at the surface is virtually disappears on the 80° trace (receiver depth=10m), and gives no interference of wave amplitudes with S* wave. Thus the S* wave can be easily discriminated. The arrival time loci for the P, PS and S* waves are indicated by the dashed and dotted lines. Since the direct P and the S* waves have expanding circular wave fronts, these loci are straight lines of constant times in the plots. Since the radius of curvature of the PS wave front varies with increasing directional angle, the travel time curve for tne reflected PS wave touches that for the S* wave at the distinct angle $\chi^*=30°=\sin^{-1}(\beta / \alpha)$ in the case of the velocity model given in Table 1. This angle marks the geometrical boundary for the region in which the S* exists.

In order to get the radiation pattern of the S* wave, the slowness integration was performed in the region of about 0.03 sec/km length to include the S* wave only. We obtain the particle motion diagrams of the wave in each receiver. Fig. 13 shows the relative amplitudes normalized by that of the wave at the receiver of 30 degrees position measured from the particle motion diagrams of the wave. In the Figure we see that the energy of the wave is the largest at the position of the distinct angle 30 degree in this velocity model structure and that the polarity reversal occurs at about 45 degrees.

Next, we construct the radiation pattern of the S* wave generated by an interface of the welded contact between the source medium and an adjacent layer of different wave propagation velocities. The model geometry for numerical computation is one layer of 200m thickness over a half space where source is located. Wave velocities of the half-space are those given in Table 1. However the velocities of the layer have two different cases, since the computational experiments are done in two ways. In the first case, lower wave velocities are assigned to the layer in such a way that the P and S wave velocities in the layer are half of those in the half-space. Secondly, higher wave velocities which are double of those in the half-space are assigned to the layer. The source is located at 5m below the interface

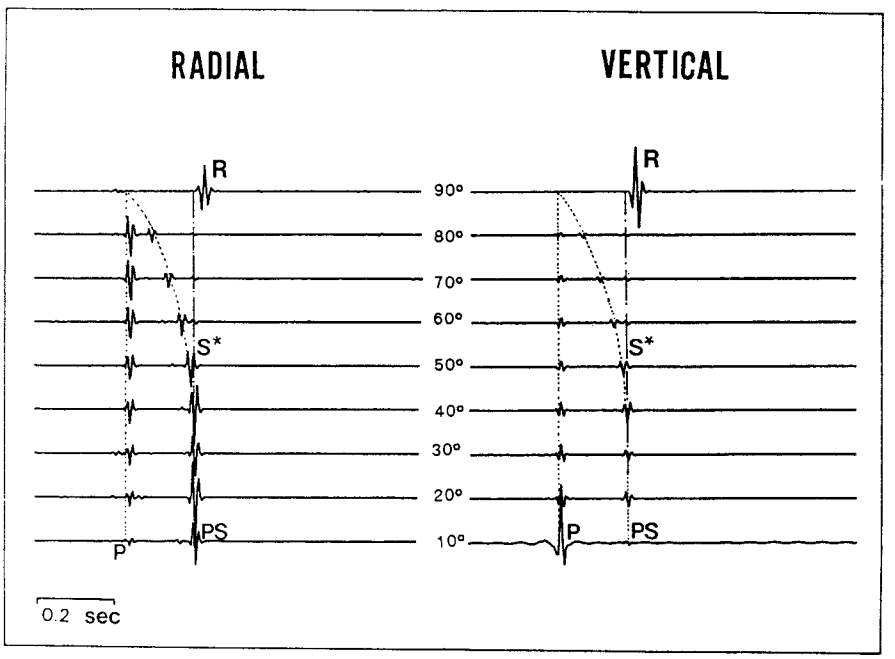

Fig. 12. Synthetic seismograms recorded by the receivers at different position designed for the radiation pattern of S*. The source is located at 5m depth. Velocity model used is given in Table 1. The receivers are distributed on quarter circle of radius 840m from the origin. The angular position of each receiver is measured from the downward vertical. The positional angel is assigned to each seismogram in degree unit. Note that the S* travel time curve ends at the distinctive angle 30 degree which marks the end of region where S* exists. R indicates the free Rayleigh wave.

of the layer and the half-space. Receiver positions are the same as those given in Fig 12. In numerical computation, a small finite slowness window of 0.04sec/km length was used in order to include the S* wave only. Results of computations are shown in Fig. 14A for the lower velocity layer case and in Fig. 14B for the higher velocity layer. The first arrival in each trace in the figure is the S* wave. Even though the slowness intergral is performed in the slowness window for the S* wave only, the inhomogeneous source wave pulse can be transmitted into the upper medium of lower wave velocities. These waves including wave to P phase propagate as homogeneous waves and reflect back into the source medium of half-space by the free surface reflections. These wave appear in Fig. 14A as later arrivals with significant amplitudes. For the case that the wave velocities of upper layer is higher than those of the source medium, these waves of the free-surface reflections does not appear in Fig. 14B. Fig. 15 displays the radiation patterns of the S* wave for the two cases. We see that the radiation pattern of the S* displayed in Fig. 15A is similar to that of Fig. 13 and polarity reversal is observed. However, the radiation pattern of the wave in Fig. 15B does not show the polarity change.

Variation of Reflection Cefficients of the S* wave

To examine the behaviour of reflection coefficients of the reflected S* wave with varying wave velocities in the medium of the other side of the interface, we use a structure model with one layer over half-space. The layer thickness is set to be 300m in order to exclude the effects caused by the free surface. The receiver is fixed at the position of epicentral distance 800m and at depth 250m from the interface in the half-space. The velocity contrast between P and S wave, V_s/V_p, is 0.5 in the two media. The source is located at 5m below from the interface in the half-space. The wave velocity ratio of the two media, V_2/V_1, varies from 0.7 to 1.3

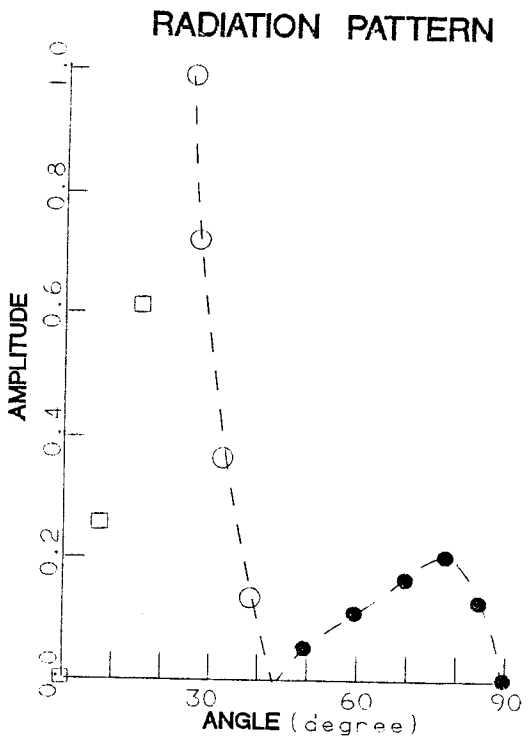

Fig. 13. Radiation pattern of the S* wave. The open circle is for the positive polarity of the wave and closed circle for negative. Three points marked by open rectangles correspond to the reflected PS wave propagating in the region where S* does not exist.

assuming the same Poisson ratio in both of the media. The subscript 1 and 2 indicate the half-space and the layer above, respectively. The relative amplitudes of the S* wave as a function of the ratio V_2/V_1 are shown in Fig. 16. In the figure, the displacement amplitude of the S* wave is normalized by that of the wave in the case of $V_2/V_1=1.3$ The larger the velocity contrast, the more the reflection coefficient of the S* wave increases. The polarity changes at the point where V_2/V_1 equals to 1.0.

Characteristics of the Transmitted "*" Waves

A velocity model with one layer of lower wave velocities over half-space in welded contact is considered for computation of the transmitted wave fields. The elastic parameters of the two media are given in Table 2. A source of compressional wave is located at depth of 2m below the interface in the half-space. Since the matrix representations of the extended reflectivity method includes the responses of the stratified media between a half-space and the free surface, we must set up the layer thicker enough to avoid the effects due to the free surface. Thus waves reflected from the free surface can be separated from direct arrivals in seismograms. There are a few non-geometrical "*" waves such as P_1P_2*, P_1S_2*, and their associated head waves in transmitted wave fields recorded in the upper medium. The subscript 1 and 2 indicate the media which waves pass through. Medium 1 refers to the lower half-space (medium of incidence) while 2 refers to upper medium where the receiver is located.

The schematic diagram for ray paths of the "*" waves in reflected and transmitted wave fields has been shown in Fig. 3. The radiation patterns of the P_1P_2* and P_1S_2* waves as a function of directional angle are dipicted in Fig. 17. The angle χ* is also given in degrees measured from the vertical axis. The distinct angle is defined by the velocity structure of the model. Slowness integration was restricted to a finite slowness window of 0.03sec/km length in order to separate the waves from other body waves in seismograms.

Synthetic seismograms for these transmitted "*" arrivals are shown in Fig. 18. An horizontal array of ten receivers is located at 20m above the interface and 200m below the free surface, so as to remove arrivals reflected from the free surface in the finite time window of seismograms. Their epicentral distances are from 550m to 1,000m with 50m interval. The point explosive source is located at 2m below the interface in the half-space. In viewing the Figure, the P_1P_1*, P_1S_2*, and $P_1p_2S_2$* waves are not found. As they have relatively less energy compared

Table 2. Parameters of the media.

MEDIUM*	P-velocity	S-velocity	density	Q-value(P)	Q-value(S)
1	4.0 km/sec	2.0 km/sec	1.0 g/cm^3	600	300
2	3.6 km/sec	1.8 km/sec	0.9 g/cm^3	500	200

* Medium 1 refers to lower half-space (medium of incidence) while medium 2 refers to upper medium where the receiver is located.

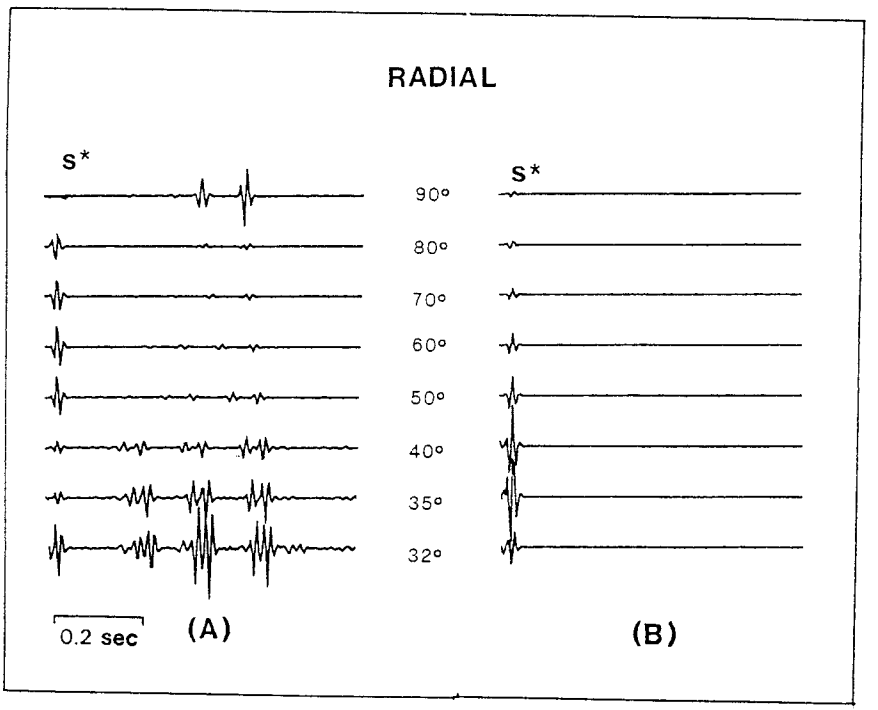

Fig. 14. Synthetic seismograms (radial traces) for the radiation patterns of the S* reflected from the interface of two elastic media. The structural model is one layer over half-space. The wavenumber integrations are performed in the slowness region of the S* wave only. The time coordinate is shifted so that the S* wave in traces are aligned as initial phases. For (A) ; The wave velocities of the upper medium are half of those of the lower medium. For (B) ; The wave velocities of the upper medium are twice of those of the lower medium. Phases of later arrival times in (A) are the contributions of transmitted "*" waves reflected from the free surface above the interface.
medium

with those of other waves in the plots of seismograms, we can not distinguish them from others. If the slowness integration is performed in the region including only these arrivals, we can detect them in the seismograms. The wave propagation velocity determined from the arrival time of the P_1S_2* phase excited at the point on the interface directly above the source is consistent with the shear wave velocity of the medium 2.

The slowness integration restricted to a finite slowness window corresponding to only two head wave type of "*" waves reveals a characteristics of amplitude decay with increasing epicentral distances. The results are depicted in Fig. 19 in semi-log scale as a function of the epicentral distance. The quantitative study will remain as the subject of further investigations.

CONCLUSION AND DISCUSSIONS

Some useful techniques for layer matrix multiplication procedure in an extended reflectivity method are developed. The usefulness of the method has been demonstrated in series of synthetic seismograms showing non-geometric "*" waves including S* in reflected and transmitted wave fields generated by the interactions of a compressional wave from a point explosive source with an interface between two elastic media or with a free surface. These non-geometric "*" waves become detectable when the point source lies closer to the boundary. As the source depth is located close to the boundary, the amplitude of the waves increases exponentially, and the linear particle motion is confined to a plane normal to the direction of propagation. The propagating shear waves seem

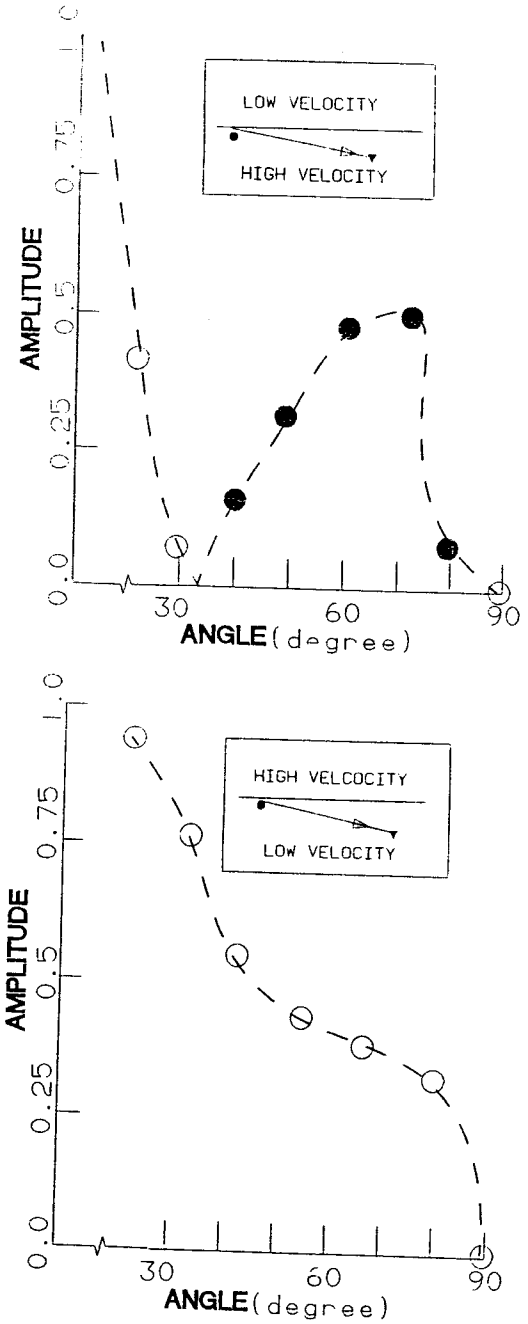

Fig. 15. Radiation patterns of S* waves from Fig. 14 (A) and (B), respectively. The open circle is for the positive polarity of displacement and closed circle for negative. The angle indicates the directional angle of rays from the downward vertical. Insets are schematic displays of sourc-receiver configurations and model geometries.

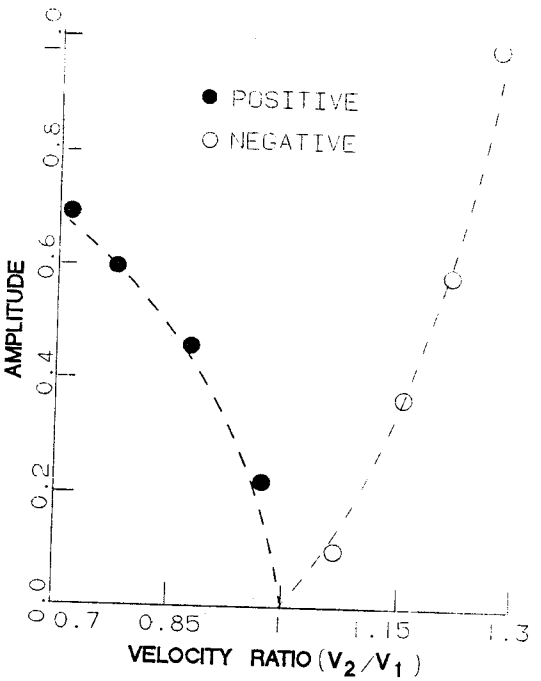

Fig. 16. Relative total displacement amplitudes of the reflected PS* waves versus the ratio V_2/V_1 where V_1 and V_2 are wave velocities of the lower and upper medium, respectively. The velocity ratio of the S wave to the P wave is set to be 0.5 in both of the medium. The closed and open circles indicate the opposite polarity of displacements.

to be excited at a point on the boundary or free surface directly above the point source.

The radiation patterns of the S* wave reveal forms such that amplitudes become zero at grazing angle, and then increases to a maximum until merging with the PS wave at distinctive angle $\chi^* = \sin^{-1}(\beta/\alpha)$. Even though the slowness integration is limited to a finite slowness window in order to obtain only reflected S* wave, other non-geometric phases were detected provided that the wave velocity of the incident wave is larger than at least one of the wave speeds on the other side of the interface. As the velocity contrasts between the source medium and the adjacent one become larger, the amplitudes of the reflected S* wave increase. This study also presents characteristics of the non-geometric "*" waves and their associated head waves including radiation patterns in transmitted wave fields.

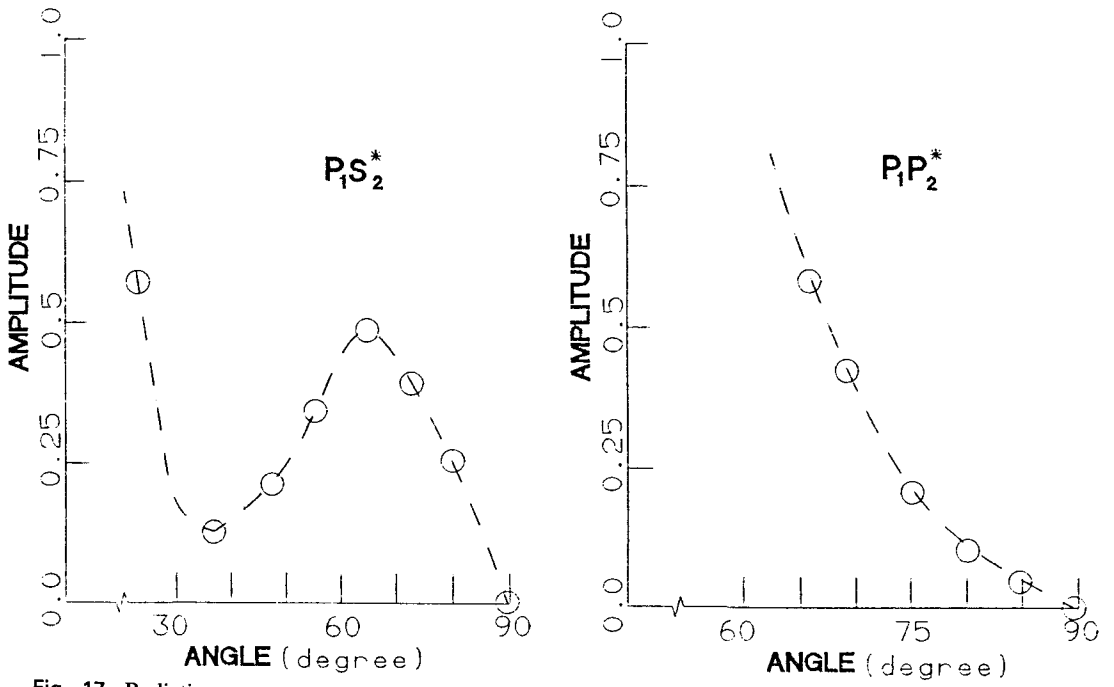

Fig. 17. Radiation patterns of the $P_1P_2^*$ and $P_1S_2^*$ waves in the upper medium. The velocity structure given in Table 2 is used. The point source is at 5m below the interface. Subscript 1 and 2 in $P_1P_2^*$ and $P_1S_2^*$ indicate the lower and upper medium of wave propagation.

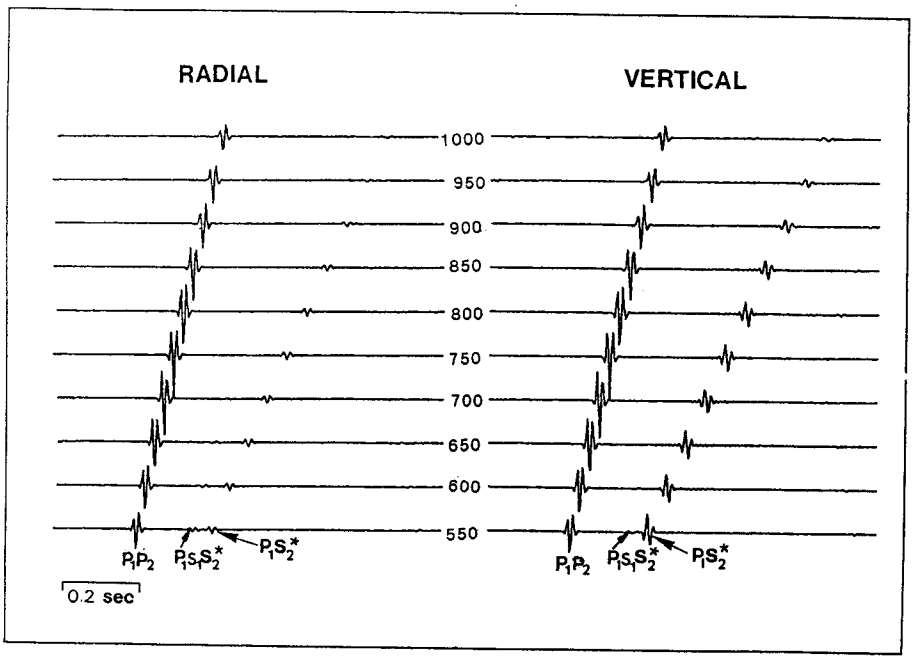

Fig. 18. Variation of seismograms of the transmitted wave fields with increasing epicentral distance. The velocity structure given in Table 2 is used. The source is located 5 m below from the interface in lower medium. The receiver array is put at depth 250m above the interface in upper medium. The number assigned to each trace is the epicentral distances. The subscript 1 and 2 indicate the medium which the ray passes through.

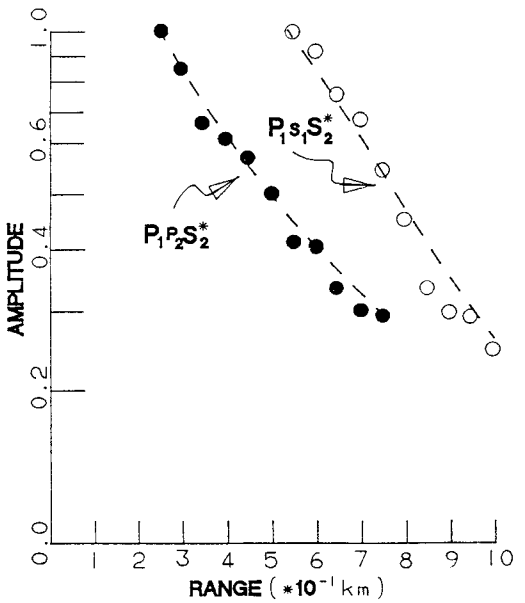

Fig. 19. Amplitude variations of the head wave type of "*" arrivals with incresaing epicentral distances. The log scale is used for the vertical axis. Velocity structure model used is given in Table 2.

Some recent detections of such waves in real data and their dominant characteristics deem such an undertaking highly desirable since most of the conventional data used in oil exploration are produced by explosive sources adjacent to interfaces of different geologic layers. The field data are consistent with the hypothesis that the interface just above the source is the excitation point of the propagating non-geometric "*" waves (Gutoeski et al., 1984). If the source is located close to a boundary in seismic vertical profiling, the non-geometrical waves may have much contributions in the amplitudes. Therefore, we point out the possibility for designing shooting procedure to produce varying degrees of the "*" waves. Such procedures will aid in designing filters which reduce the amplitudes of the waves as noise and in identifying P and S waves which contain the information of the subsurface geologic structure. Additionally the non-geometric "*" waves can also be used for independent information about the medium, since the charcaters of the "*" waves such as the amplitude decay with source depth, radiation pattern, and polarity etc. depend on physical property of the medium.

REFERENCES

Abo-zena, A. (1979) Dispersion function computation for unlimited frequency value. Geophys. J. R. Astr. Soc., v. 58, p. 91-105.

Aki, K. and Richards, P. G. (1980) Quantitative Seismology : Theory and Methods., v. 1, W. H. Freeman Company, San Francisco.

Alekseev, A. S. and Mikhailenko, B. G. (1980) The solution of dynamic problems of elastic wave propagation in inhomogeneous media by a combination of partial separation of variables and finite difference methods. J. Geophys., v. 48, p. 161-172.

Alford, R. M., Kelly, K. R., and Boore, D. M. (1974) Accuracy of finite difference modeling of the acoustic wave equation. Geophysics, v. 39, p. 834-842.

Alterman, Z. and Loewendthal, D. (1972) Computer generated seismograms, in Methods in Computational Physics. v. 12, (eds). B. A. Bolt, B. Alder and M. Rotenberg, Academic Press, New York.

Baag, C.E. and Baag, C. (1988) An extended reflectivity method for the P-SV-Rayleigh wave system : Theory, Jour. Geol. Soc. Korea, v. 24, p. 489-499.

Boore, D. M. (1972) Finite difference methods for seismic wave propagation in heterogeneous materials, in Methods in Computational Physics. v. 11, (eds). B. A. Bolt, B. Alder and M. Rotenberg, Academic Press, New York.

Bortfeld, R. K. and Fertig, J. (1982) On the importance of the shear wave S* for seismic prospecting, PREUSSAG Technical Report. Hannover. (in German).

Daley, D. F. and Hron, F. (1983a) High-frequency approximation to the nongeometrical S* arrival. Bull. Seism. Soc. Am., v. 73, p. 109-123.

Daley, D. F. and Hron, F. (1983b) Nongeometric arrivals due to highly concentrated sources. Bull. Seism. Soc. Am., v. 73, p. 1655-1671.

Fuchs, K. (1968) Das reflexions und Transmissionsvemogeneines geschichteten Mediums mit beliebiger Tiefen-Verteilung derelastichen Moduln und Dichte fur schragen Einfall ebener Wellen. Z. Geophys., v. 34, p. 389-413.

Fuchs, K. and Muller, G. (1971) Computation of synthetic seismograms with the reflectivity method and comparison with observations. Geophys. J. R. astr. Soc., v. 23, p. 417-433.

Gutowski, P. R., Hron, F., Wagner, D. E. and Treitel, S. (1984) S*. Bull. Seism. Soc. Am., v. 74, p. 61-78.

Harkrider, D. G. (1964) Surface waves in multilayered elastic media, Part I. Rayleigh and Love waves from buried sources in a multi-layered elastic half-space. Bull. Seism. Soc. Am., v. 54, p. 627-679.

Harkrider, D. G. (1970) Surface waves in multilayered elastic media, Part II. Higher modes spectra and spectral ratios from point sources in plane layered earth models. Bull. Seism. Soc. Am., v. 60, p. 1937-1987.

Haskell, N. A. (1953) Dispersion of surface waves on multilayered media. Bull. Seism. Soc. Am., v. 43,

p. 17-34.
Haskell, N. A. (1960) Crustal reflection of plane SH waves. J. Geophys. Res., v. 65, p. 4147-4150.
Haskell, N. A. (1962) Crustal reflection of plane P and SV waves. J. Geophys. Res., v. 67, p. 4751-4767.
Hron, F. and Mikhailenko, B. G. (1981) Numerical modelling of non-geeometrical effects by the Alekseev-Mikhailenko method. Bull. Seism. Soc. Am., v. 71, p. 1011-1029.
Kelly, K. R., Ward, R. W., Treitel, S. and Alford, R. M. (1976) Synthetic seismograms : a finite difference approach. Geophysics, v. 41, p. 2-27.
Kim, J. Y. and Behrens, J. (1985) The existence of the S* wave experimentally proved by means of model-seismic investigations, in Seismic Shear Waves, v. 15, Geophysical Press, Amsterdam.
Kim, J. Y. and Behrens, J. (1986) Experimental evidence of S*-wave. Geophys. Prospect. v. 34, p. 100-108.
Kind, R. (1978) The reflectivity method for a buried source. J. Geophys., v. 44, p. 603-612.
Lapwood, E. R. (1949) The disturbance due to a line source in a semi-infinite elastic medium. Phil. Trans. Roy., Soc. Lond., v. A 242, p. 63-100.
Mikhailenko, B. G. and Hron, F. (1980) Discovery of a new non-geometrical S* arrival generated at the free surface, in Abstracts of the Joint EGS-ESC Meeting, Budapest, 188.
Sandmeier, K.J. and Wenzel, F. (1985) Synthetic seismograms for a complex crustal model. Geophys. Res. Lett., v. 12, p. 22-25.
Watson, T. H. (1970) Fast computation of Rayleigh wave dispersion in a layered half-space. Bull. Seism. Soc. Am., v. 60, p. 161-166.

Manuscript received 29 August 1990.

반사도 기법에 의한 비기하적 S* 및 P* 파의 합성 계산

홍 동 희·박 창 업

요약 : 비기하적 S*및 P*파를 계산하고 그들의 특징적 성질을 추론하였다. 이들 파는 점진원의 불균질성 P파에 의해 매질의 자유표면 또는 두 매질사이의 접촉면에서 발생하여 매질 속을 균질성 S파 또는 P파로서 전파된다. 진원점과 수진점이 지표면이 아니라, 지하 깊이에 위치해 있을 때에도 계산이 가능하도록 만들어진 반사도 기법을 이용하여 이들 파의 합성지진파를 계산하였다. 이 계산과정에서 각 매질층에 대한 전파행렬식을 효과적으로 계산하는 방법을 제시하여 계산시간과 컴퓨터의 필요한 기억용량을 줄일 수 있도록 하였다. 계산된 합성지진파로부터 자유면에서 발생한 S*파와, 매질 접촉면에서 발생한 반사 S*파, 투과 S*파 및 투과 P*파에 대한 방사양상을 산출하였다. 여러 방사방향에 대한 이들 파동의 변위변화는 극의 반전, 진폭의 단순감쇠 및 비단순변화등의 현상이 속도구조에 따라서 다르게 나타났다. 선두파 형식의 S*및 P*파에 대해서는 수진점 거리증가에 따른 진폭감쇠 정도를 유추하였다.